CHIRP OPTICAL COHERENCE TOMOGRAPHY OF LAYERED SCATTERING MEDIA

U. H. P. Haberland, V. Blazek, and H. J. Schmitt
Institute of High Frequency Technology, Melatener Str. 25, 52056 Aachen, Germany

ABSTRACT

A new noninvasive technique that reveals cross sectional images of scattering media is presented. It is based on a continuous wave frequency modulated radar, but uses a tunable laser in the near infrared. As the full width at half maximum resolution of 16 μm is demonstrated with an external cavity laser, the chirp optical coherence tomography becomes an alternative to conventional short coherence tomography with the advantage of a simplified optical setup. The analysis of two-layer solid phantoms shows that the backscattered light gets stronger with decreasing anisotropic factor and increasing scattering coefficient, as predicted by Monte Carlo simulations. By introducing a two-phase chirp sequence, the combination of lateral resolved perfusion and depth resolved structure is shown. © *1998 Society of Photo-Optical Instrumentation Engineers.* [S1083-3668(98)00503-6]

Keywords optical coherence tomography; scattering media; tunable laser; skin imaging; Monte Carlo simulation.

1 INTRODUCTION

Over the last years optical coherence tomography has become a tool of increasing interest if high resolution cross sectional images of biotissues are required. Applications include the investigation of skin cancer, ophthalmological structures such as anterior chamber and fundus layers, and endoscopic accessible tissues.[1,2] Most of these devices use broadband light sources, e.g., superluminescence diode (SLD), with a short coherence time and they need a scanning mirror to record the depth resolved backscattered signal.

In this article we present a novel imaging technique that is based on a tunable laser. Instead of moving the mirror, the wavelength of the laser can be varied electronically to record the backscattered signal. This principle has been used extensively in frequency modulated continuous wave (FMCW) radars since it became declassified in 1960. In optics it helps the analysis of passive optical networks and integrated optical devices[3–5] which consist of several discrete reflection sites.

The first part of this article explains the working principle and the signal processing to obtain cross sectional images of scattering media. The characteristics of two different types of tunable laser are investigated and the experimental arrangement of our chirp optical coherence tomograph (C-OCT) is described. With these C-OCT different kinds of stratified scattering objects are measured and compared to simulation results. The last part concentrates on the effect of moving scatterers on tomographic and functional imaging.

Address all correspondence to U. H. P. Haberland. E-mail: udo@ihf.rwth-aachen.de

2 PRINCIPLE AND THEORY

A laser, whose oscillator frequency is swept linear with time, irradiates into a Michelson interferometer (Figure 1). One arm of the interferometer is terminated by a fixed mirror, while the other arm is attached to the object under investigation. The light reflected from the mirror and from the object are superimposed on the detector. The coherence length of the laser is larger than the path length difference by several orders of magnitude. Hence the two waves interfere coherently with the detector. As the propagation times of the reflected waves are different, the waves that reach the detector simultaneously have been launched into the interferometer at different times. Due to the linear frequency modulation of the laser the frequencies of the interfering waves differ by an amount proportional to the path length difference. After the PIN photodiode only the low frequency beat spectrum is observed. In the case of a single reflection of the object the peak of the beat spectrum gives the position of the object with respect to the fixed mirror. In volume scattering objects the light penetrates into the object and returns via many different paths. The dependence of the backscattered light on photon propagation path length can be obtained from the spectrum of the detector signal.

2.1 THEORY

In the following treatment no polarization effects are considered. The transmitted field at the output of the interferometer is given by the superposition of the field $E_{ref}(t)$ returned by the reference mirror and all backscattered fields from the object $E_{obj}(t)$.
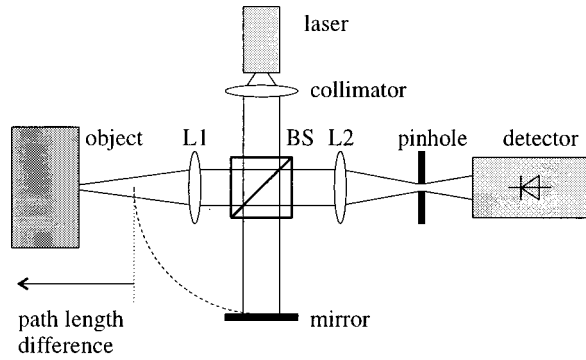
Fig. 1 Principle setup of the chirp optical coherence tomography; (BS) beamsplitter, (L1,L2) lens.

The latter one can be described by the complex amplitude reflection coefficient $r(\tau)$, with τ being the difference in propagation time between the interferometer arms. Thus $E_{\text{obj}}(t)$ is given by

$$E_{\text{obj}}(t) = \int_0^\infty r(\tau)E(t-\tau)d\tau. \tag{1}$$

Any further attenuation by the beam splitter can be ascribed to $r(\tau)$. Neglecting a constant factor, the transmitted power P_T can be written as

$$P_T(t) = [E_{\text{ref}}(t) + E_{\text{obj}}(t)]^*[E_{\text{ref}}(t) + E_{\text{obj}}(t)]$$
$$= [E_{\text{ref}}^*(t)E_{\text{ref}}(t) + E_{\text{obj}}^*(t)E_{\text{obj}}(t)]$$
$$+ 2\,\text{Re}\,[E_{\text{ref}}^*(t)E_{\text{obj}}(t)]. \tag{2}$$

The emitted field of the laser has an instantaneous frequency ν that is modulated by a sawtooth function. During the rising portion of the modulation function the laser field can be described by

$$E(t) = e^{j\phi(t)} = e^{j(w_0 t + 0.5\alpha t^2)} \tag{3}$$

with the instantaneous frequency

$$\nu(t) = \frac{1}{2\pi}\frac{d\phi}{dt} = \frac{1}{2\pi}(w_0 + \alpha t), \tag{4}$$

where $\alpha/2\pi$ is the chirp rate. Evaluation of Eq. (2) yields for the first term

$$E_{\text{ref}}^*(t)E_{\text{ref}}(t) = e^{-j\phi(t)}e^{j\phi(t)} = 1 \tag{5}$$

and the second term is given by

$$E_{\text{obj}}^*(t)E_{\text{obj}}(t) = \left| \int_0^\infty r(\tau)e^{j[w_0(t-\tau)+0.5\alpha(t-\tau)^2]}\,d\tau \right|^2$$
$$= \left| \int_0^\infty r(\tau)e^{j(-w_0\tau+0.5\alpha\tau^2-\alpha\tau t)}\,d\tau \right|^2.$$

As the propagation time different τ is on the order of 10^{-10} s and the smallest measurement time is about 10^{-5} s, the exponent can be simplified using $0.5\alpha\tau^2 \ll \alpha\tau t$:

$$E_{\text{obj}}^*(t)E_{\text{obj}}(t) = \left| \int_0^\infty r(\tau)e^{-j(w_0+\alpha t)\tau}\,d\tau \right|^2. \tag{6}$$

The integral represents the Fourier transformation of $r(\tau)$, if the instantaneous frequency ν is used:

$$E_{\text{obj}}^*(\nu)E_{\text{obj}}(\nu) = \left| \int_0^\infty r(\tau)e^{-j2\pi\nu\tau}\,d\tau \right|^2 = |R(\nu)|^2. \tag{7}$$

The third term of Eq. (2) can be evaluated under the same assumptions as above:

$$E_{\text{ref}}^*(\nu)E_{\text{obj}}(\nu) = \int_0^\infty r(\tau)e^{-j2\pi\nu\tau}\,d\tau = R(\nu). \tag{8}$$

Substituting Eqs. (6), (7) and (8) back into (2) gives

$$P_T(\nu) = 1 + |R(\nu)|^2 + 2\,\text{Re}\{R(\nu)\}. \tag{9}$$

Since the interferometer can be adjusted in such a way that $r(\tau)$ is zero for values $\tau < 0$, $r(\tau)$ can be expanded to a symmetric function $r(-\tau) = r(\tau)$. As $r(\tau)$ is now symmetric, its Fourier transform is real, leading to

$$P_T(\nu) = 1 + |R(\nu)|^2 + 2R(\nu). \tag{10}$$

Using a photodetector, the photocurrent $I(\nu)$ is proportional to transmitted light power $P_T(\nu)$. Its inverse Fourier transform,

$$J(\tau) = \int_{-\infty}^\infty I(\nu)e^{j2\pi\tau\nu}\,d\nu, \tag{11}$$

can be calculated:

$$J(\tau) = \delta(\tau) + \phi_{rr}(\tau) + 2r(\tau). \tag{12}$$

The Fourier transformation of the photocurrent with respect to the instantaneous frequency gives the autocorrelation $\phi_{rr}(\tau)$ of the amplitude reflection coefficient $r(\tau)$. The Dirac function $\delta(\tau)$ stands for the dc component of the detector signal. The temporal spread of the object reflections $r(\tau)$ is limited to an interval $\tau_0 < \tau < \tau_0 + \tau_{\text{max}}$, with τ_0 being the delay of the surface reflections of the object with respect to the mirror. If the reference mirror is positioned to obey the relation $\tau_0 > \tau_{\text{max}}$, the autocorrelation $\phi_{rr}(\tau)$ can be separated from $r(\tau)$. The influence of a nonlinear chirp and frequency noise on the detector signal has been discussed before.[6,7]

2.2 SPATIAL RESOLUTION

The spatial resolution is determined by the frequency resolution of the measured detector signal. The measurement takes place during the time T the sawtooth modulation signal rises. The frequency resolution is thus given by $\delta f = 1/T$. Under the simplifying assumption that the object just consists of a single reflection site at path length imbalance z, the
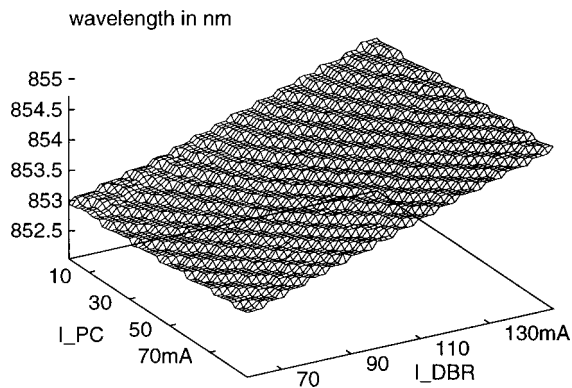
Fig. 2 Tuning profile of YL85XTW electrically tunable semiconductor laser. The modulation currents in the PC and DBR section were varied.

Fig. 3 Interference signal of a Michelson interferometer illuminated by an external cavity laser swept from 771 to 791 nm wavelength.

detector signal exhibits a sinusoidal oscillation at the beat frequency $f_{beat} = \alpha z / \pi c$, where $\tau = 2z/c$ gives the relation between path length imbalance and propagation time difference (c: speed of light in material). The total frequency deviation (tuning range) during the measurement interval T is further given by $\Delta \omega = \alpha T$. The spatial resolution just depends on the tuning range:

$$\delta z = \frac{c \pi}{\Delta \omega}. \qquad (13)$$

To achieve a high resolution a large tuning range is required. The resolution is independent of the tuning time.

3 TUNABLE LASER

A tunable laser plays the key role in the design of an optical chirp system. The main requirements of the laser source are wide tuning range to yield a good spatial resolution and short tuning time to reduce the duration of the measurements. The two most promising laser types have been characterized with respect to their use in C-OCT.

3.1 THREE SECTION LASER DIODE

An electrically tunable laser diode composed of three elements is now available at 852 nm central wavelength. By applying currents through the two tuning sections [phase control (PC), distributed Bragg reflection (DBR)] the emitted wavelength can be changed as shown in Figure 2. The current through the DBR section changes the effective grating pitch, which basically determines the wavelength that is reflected back into the active unit. The PC section induces a phase delay inside the cavity, which can be modulated by the PC current to adjust the optical cavity length in accordance with the emitted wavelength. A tuning behavior without any frequency hops was obtained by varying the tuning currents simultaneously to stay on one of the plateaus. The driving currents are modulated in
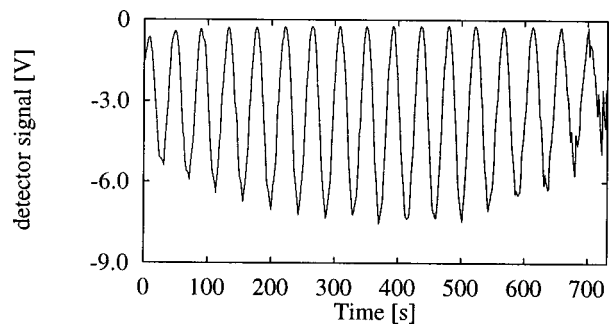
such a way that the instantaneous frequency of the laser increases linear with time.[7] With that driving principle the laser was tuned by 0.8 nm in 5 ms with a mean output power of 6 mW.

3.2 EXTERNAL CAVITY LASER

A larger tuning range at the expense of a longer tuning time exhibits the external cavity laser. A single sided anti-reflex coated laser diode illuminates a diffractive grating; hence the laser cavity is terminated by the uncoated facet and the grating. The laser operates on the wavelength that is reflected back from the grating into the diode. By continuously tilting the grating, the wavelength that is reflected back into the gain medium is altered. Thus the instantaneous frequency the laser operates on can be changed by the position of the grating. Feeding the emitted light into a common Michelson interferometer shows the expected sinusoidal detector signal during the tuning process (Figure 3). The envelope corresponds to the gain spectra of the active semiconductor material. After Fourier transformation of the detector signal the full width at half maximum of the main peak (Figure 4) gives a spatial resolution of 16 μm. This value corresponds well with the expected theoretical resolution of 15.2 μm given by Eq. (13), with a tuning range of 20 nm at the center wavelength 780 nm. That type of laser improves the resolution of the C-OCT which be-
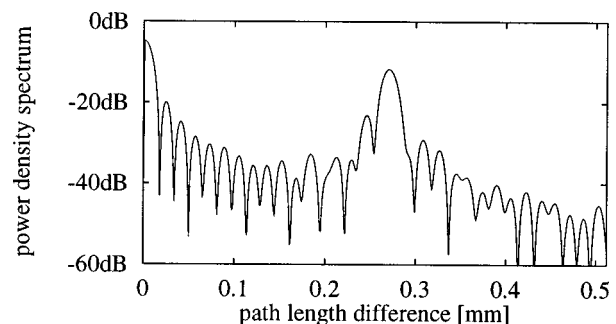

Fig. 4 Spectrum of the detector signal shown in Fig. 3. The full width at half maximum is 16 μm; frequency space has been mapped to path length distances by using $f_{beat} = \alpha z / \pi c$.

comes comparable to short coherence interferometry with SLDs while offering an optical power of 10 mW. As the external cavity laser exhibits mode hops during tuning, the interference signal at the detector exhibits phase jumps, which are responsible for a limited dynamic range. From Figure 4 the peak above noise flow value is 15 dB.

4 EXPERIMENTAL SETUP AND SIGNAL PROCESSING

All measurements were performed with the optical setup shown in Figure 1. Because of the limited dynamic range of the ECL system and to reduce measurement time, only the three-section laser diode was used in the experiments on scattering media. Hence the spatial resolution of the presented tomograms is limited to 453 μm according to the 0.8 nm tuning range at 852 nm center wavelength. A low numerical aperture (NA) lens (NA = 0.20) focused the collimated laser beam into the phantom at a focal depth of 2 mm. The second lens with the same NA collected the backscattered and reflected light to the pinhole of the diameter 300 μm in front of the detector. The object was tilted by 3° to reduce specular surface reflection that may saturate the detector. The signal from the PIN photodiode was subsequently bandpass filtered (1.5–20 kHz) and amplified before quantization. The obtained sequence was filtered by a Hanning window to reduce side-lobes prior to the Fourier transformation. From the power spectrum of the filtered backscattered signal a single line (A scan) of the tomogram was generated by gray color coding. A scans from successive lateral displaced positions of the object were combined to yield a full two-dimensional (2D) tomogram. No image reconstruction algorithm was needed. The lateral displacement between each scan was 168 μm.

The measurements were performed on solid scattering phantoms that were produced according to a recipe by Delpy[8] and Rinneberg.[9] They consist of silica spheres embedded into a clear resin (refractive index: $n = 1.39$ at 780 nm). The anisotropic factor g and the scattering coefficient μ_s could be chosen by varying sphere size and concentration.

5 LAYERED MEDIA

The human skin consists of a stratified tissue where the layers differ by their scattering coefficients and anisotropic factors. Two experiments were performed on solid scattering phantoms that are composed of two layers.

5.1 MEASUREMENTS ON LAYERED MEDIA

In a first experiment a phantom with two layers of different scattering coefficient but the same anisotropic factor was used. As shown in Figure 5 the low scattering upper layer ($\mu_s = 0.3$ mm^{-1}, $g = 0.78$) had a linear varying thickness from 0 to 9 mm
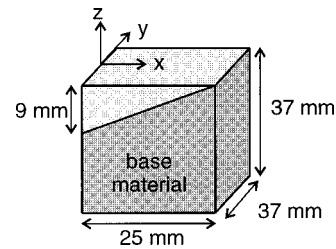

Fig. 5 Structure of the phantoms with a wedge-shaped upper layer.

depth over 25 mm that was placed on top of a strongly scattering base material ($\mu_s = 5.1$ mm^{-1}, $g = 0.78$). The tomogram was recorded by 150 A scans along the y axis with a total beam displacement of 25 mm.

The measured tomogram (Figure 6) exhibits a horizontal interrupted bright line that corresponds to the diffuse reflection at the air–phantom interface. Below that line a darker area of increasing thickness is found that is limited by a bright band that diminishes with increasing distance from the surface of the object. A comparison between the tomogram and the phantom sizes points out a good agreement of the dark area to the low scattering upper layer. The interface between the two layers can be traced to a geometrical depth of approximately 8 mm inside a scattering medium with $\mu_s = 0.3$ mm^{-1}.

In a second experiment a phantom with the same dimensions and structure was used. Now the upper layer had a lower anisotropic factor ($g = 0.33$) than the base material ($g = 0.78$) while the scattering coefficients of the layers were the same ($\mu_s = 0.3$ mm^{-1}). The corresponding tomogram (Figure 7) shows the bright horizontal line that is given by the surface reflection. Below that line a wedge-shaped bright area reveals the position of the upper layer with the low anisotropic factor. Those parts that are further away from the wedge
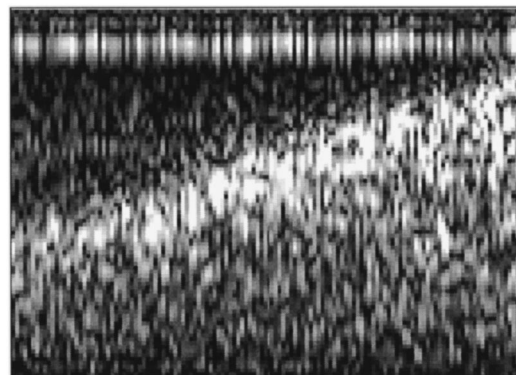

Fig. 6 Cross sectional image of a solid phantom that consists of a wedge-shaped upper layer with smaller scattering coefficient than the base material.
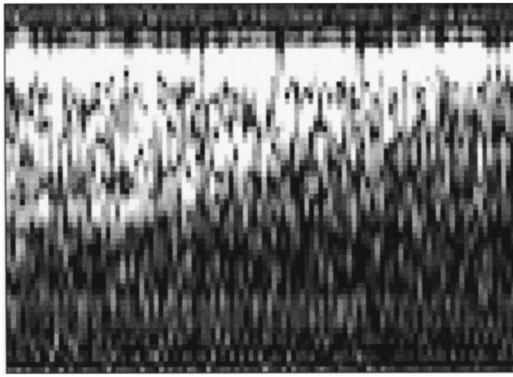
Fig. 7 Cross sectional image of a solid phantom that consists of a wedge-shaped upper layer with smaller anisotropic factor than the base material.

Fig. 8 Simulated TPSF of a two layer material with an upper layer of 4 mm thickness and lower scattering coefficient than the base material.

appear dark; the residual horizontal lines are due to multiple reflections inside the interferometric setup.

5.2 SIMULATION ON LAYERED MEDIA

Light propagation in the interferometer and scattering material was analyzed by Monte Carlo simulations and ray-tracing. The illuminating and detecting optical system was simplified by an equivalent confocal geometry similar to the one described by Schmitt et al.[10] In the simulation the equivalent focus length and diameter of the confocal lens is twice the objective lens data (objective lens: diameter 25 mm, focal length 60 mm, depth of focus 2 mm underneath the objects surface). Beam propagation outside the scattering material was performed in a paraxial approximation. The photons inside the object were treated by the Monte Carlo algorithm[11] assuming a Henyey–Greenstein phase function. Photon tracking was terminated if either the photon leaves the object without propagation towards the detector or the total photon path length exceeds 16 mm.

The simulated object consists of an upper layer of thickness 4 mm on top of a base material (second layer). The overall size of the object was $25 \times 37 \times 37$ mm^3. The scattering properties of the layers were chosen according to their experimental counterpart.

The temporal point spread function (TPSF) presented in Figure 8 is based on a simulation with the same low scattering upper layer ($\mu_s = 0.3$ mm^{-1}, $g = 0.78$) and the strong scattering second layer ($\mu_s = 5.1$ mm^{-1}, $g = 0.78$) as used in the first experiments. After photon propagation of 8 mm inside the object, an enhanced backscattered signal is obtained. The steep rise at a path length of 8 mm demonstrates the good spatial resolution despite multiple scattering. The number of scattering processes that a photon had experienced before detection depends on the pinhole of the detector. It has been demonstrated elsewhere that a pinhole of 0.3
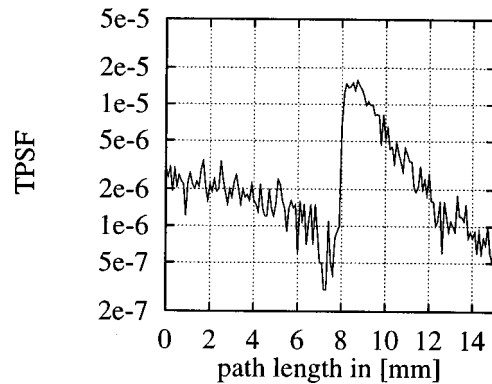
mm basically detects photons that have been scattered 1–3 times.[12]

A second simulation shows the TPSF of a layered medium with the same scattering coefficients and anisotropic factors as used in the second experiment. In this case the backscattered signal drops sharply after 8 mm photon path length (Figure 9). Although the spatial spread of the incoming beam is expected to be larger due to the low anisotropic factor in the upper layer, the signal drops sharply at the layer's boundary.

Comparison between simulation and experiments shows excellent agreement as long as the illumination and detecting optical system is considered. However, the tomograms show a speckled appearance that cannot be explained by the incoherent Monte Carlo simulation. The simulated TPSF can therefore be interpreted only as an envelope of the measured signal.

6 SCATTERING LIQUIDS

So far only static objects have been discussed. In biotissues scattering liquids like blood contain moving scatterers, e.g., red blood cells, that induce a Doppler spread on the backscattered light. This
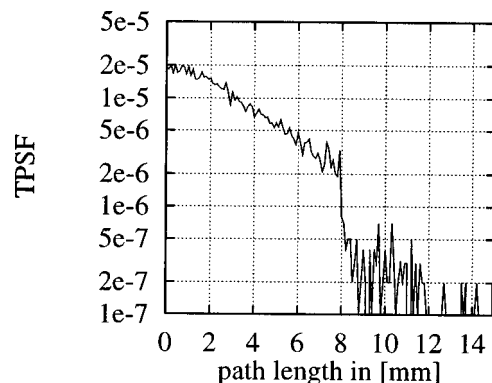

Fig. 9 Simulated TPSF of a two layer material with an upper layer of 4 mm thickness and lower anisotropic factor than the base material.
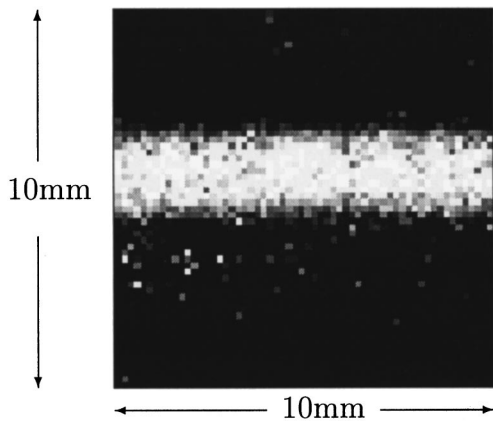
Fig. 10 Lateral resolved laser Doppler perfusion map of a scattering liquid running through a tube inside a solid scattering phantom.

Doppler spread can be used to monitor blood perfusion (laser Doppler perfusion imaging, LDPI)[13] and it affects the C-OCT images as will be shown below.

6.1 FUNCTIONAL IMAGING

Optical coherence tomography visualizes the scattering properties of the tissue under investigation. Besides this morphological knowledge the amount of blood perfusion plays an important role to access tissue functionality. The principle of LDPI can be easily incorporated into the C-OCT system by introducing a two-phase chirp sequence.

During the first phase the laser's frequency is not modulated. The interference of photons scattered at static scatterers and reflected by the mirror with those photons scattered at moving red blood cells results in a Doppler spread of the reflected light. The power density spectrum $|S(f)|^2$ of the detector signal is evaluated by the method described by Nilsson et al.:[13]

$$PU = \int_0^\infty f|S(f)|^2 \, df. \tag{14}$$

The obtained perfusion units (PUs) give a value that represents the local perfusion. By moving the object across the beam, a laterally resolved perfusion map can be built up.

Measurements were performed on a solid scattering phantom ($\mu_s = 0.3$ mm^{-1}, $g = 78$) with a hole of diameter 3 mm drilled 5 mm underneath the sur-

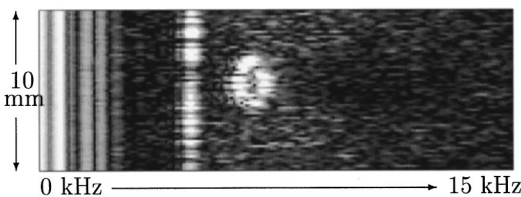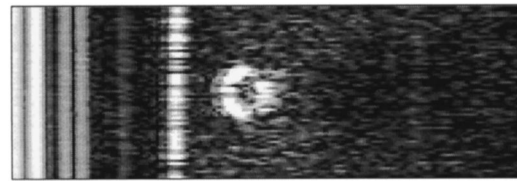**Fig. 11** Tube filled with air.

Fig. 12 Tube filled with water, flow: 0 ml/min.

face. A scattering liquid (diluted milk: $\mu_s = 8.55$ mm^{-1}) was running through the pipe at a constant flow of 0.77 ml/min. Assuming a parabolic velocity profile for a laminar flow, a maximal velocity in the center of the pipe of 3.6 mm/s can be calculated from $v_{max} = 2I/\pi R^2$ ($I = 0.77$ ml/min, $R = 1.5$ mm).

The recorded gray color coded perfusion map (Figure 10) clearly indicates the position of the pipe inside the resin. If the point of illumination is laterally displaced from the pipe, the reflected light can still exhibit a Doppler spread because light spreads out in scattering tissues and some photons are scattered within the pipe. Therefore the appearing lateral size of the region of high perfusion is larger than the physical size of the pipe.

6.2 DOPPLER SPREAD

The aim of this section is to demonstrate the effect of moving scatters on the recorded cross sectional images. In the second phase a tomogram is recorded as described in Sec. 4. No information from the first phase is used in the signal processing. According to the depth of moving scatterers, the Doppler spread is frequency shifted by that beat frequency one would obtain if no movement takes place. If no *a priori* information about the static scatterers is available, a separation between Doppler spread and the beat frequencies cannot be achieved. The influence of moving scatterers is demonstrated in the cross sectional images of the scattering phantom that have been used for LDPI in Sec. 6.1.

Figure 11 shows the tomogram in the case of an empty pipe. The vertical line is caused by the object's surface; the inner ellipse results from the rough border of the drilled pipe. After filling the pipe with water, the optical distance in the tube increases. The reflection from the deeper parts of the tube wall are shifted to higher beat frequencies (Figure 12). If the water is replaced by the scattering liquid (diluted milk: $\mu_s = 8.55$ mm^{-1}) the ellipse in the corresponding tomogram (Figure 13) gets filled.
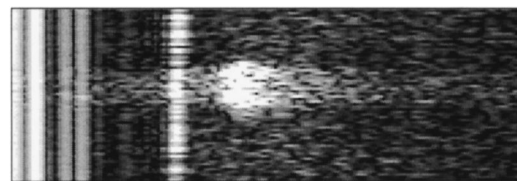

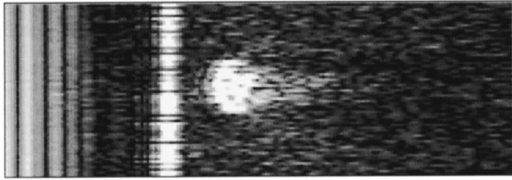
Fig. 13 Tube filled with diluted milk; flow: 0 ml/min.

Fig. 14 Tube filled with solid rod.

Fig. 16 Tube filled with diluted milk; flow: 1.375 ml/min.

Furthermore it elongates to higher and lower frequencies. As the direction of illumination is perpendicular to the pipe, the axial Doppler spread is symmetric about the position of the static reflection of the pipe. But an asymmetric elongation to higher frequencies appears even at no net flow as demonstrated in Figure 14. An explanation can be found by recording the tomogram with a pipe filled with solid scatterers with the same scattering coefficient as the liquid. A pronounced elongation to higher frequencies due to multiple scattering that enlarges the photon path length is shown in Figure 14. Therefore the asymmetry can be explained by the effect of multiple scattering superimposed on the Doppler spread. Even with no net flow a Doppler spread occurs because of Brown's molecular movement.

With increasing flow inside the pipe the axial spread increases (Figures 15 and 16). As the energy of the Doppler spreaded photons are smeared out over a larger frequency space, the static reflection becomes visible again at higher flow rates (Figure 16).

The width of Doppler spread Δf_d depends on the velocity of the scatterers and the central wavelength, but it is independent of the tuning time. Hence shortening the tuning time T reduces the spatial axial spread because the ratio of frequency resolution and Doppler spread $(1/T)/\Delta f_d$ increases.

7 CONCLUSION

With the availability of broadly tunable lasers chirp optical coherence tomography is a promising candidate for high resolution imaging in turbid media. It was demonstrated on wedge-shaped two-layer solid phantoms that a change in the scattering coefficient by a factor of 15 could be traced up to a depth of 2.4 mean free path length. Furthermore scattering layers could be differentiated by their an-
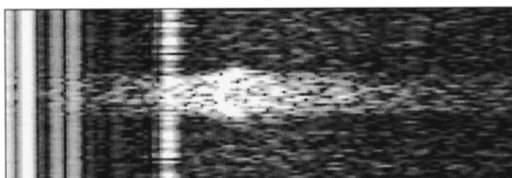
isotropic factor. A top layer with an anisotropic factor smaller by 2.6 compared to the base layer exhibited a pronounced backscattered signal. These results are in agreement with Monte Carlo simulations that took the illumination and detection into account.
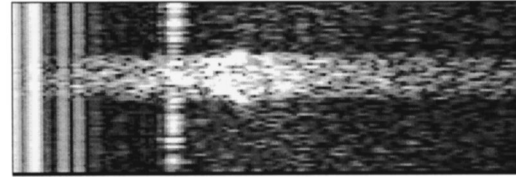
Alternative chirp sequences offer opportunities to deal with moving scatterers. Using a two-phase chirp, the Doppler spread yielding perfusion parameters was evaluated while the laser frequency remained constant (phase 1). A subsequent linear chirp (phase 2) imaged the tissue structures.

Future work will concentrate on movement artifact reduction by new chirp sequences and is aimed at improved spatial resolution.

REFERENCES

1. J. Wilkins, C. Puliafito, M. Hee, J. Duker, E. Reichel, J. Coker, J. Schuman, E. Swanson, and J. Fujimoto, "Characterization of epiretinal membranes using optical coherence tomography," *Ophthalmology* **103**, 2142–2151 (1996).
2. W. Drexler, C. Hitzenberger, H. Sattmann, and A. Fercher, "Measurement of the thickness of fundus layers by partial coherence tomography," *Opt. Eng.* **34**, 701–709 (1995).
3. H. Barfuss and E. Brinkmeyer, "Modified optical frequency domain reflectometry with high spatial resolution for components of integrated optic systems," *J. Lightwave Technol.* **7**, 3–10 (1989).
4. U. Glombitza and E. Brinkmeyer, "Coherent frequency-domain reflectometry for characterization of single-mode integrated-optical waveguides," *J. Lightwave Technol.* **11**, 1377–1384 (1993).
5. R. Passy, N. Gisin, and J. von der Weid, "High-sensitivity-coherent optical frequency-domain reflectometry for characterization of fiber-optic network components," *Photon. Technol. Lett.* **7**, 667–669 (1995).
6. U. Haberland, W. Rütten, V. Blazek, and H. Schmitt, "Investigation of highly scattering media using near-infrared continuous wave tunable semiconductor laser," in *Optical Tomography and Photon Migration, Proc. SPIE* **2389**, 503–512 (1995).
7. U. Haberland, P. Jansen, V. Blazek, and H. Schmitt, "Optical coherence tomography of scattering media using frequency modulated continuous wave techniques with tunable near-infrared laser," in *Coherence Domain Optical Methods in Biomedical Science and Clinical Applications, Proc. SPIE* **2981**, 20–28 (1997).
8. M. Firbank and D. Delpy, "A design for a stable and reproducible phantom for use in near infra-red imaging and spectroscopy," *Phys. Med. Biol.* **38**, 847–853 (1993).
9. U. Sukowski, F. Schubert, D. Grosenick, and H. Rinneberg, "Preparation of solid phantoms with defined scattering and

Fig. 15 Tube filled with diluted milk; flow: 0.88 ml/min.

absorption properties for optical tomography,'' *Phys. Med. Biol.* **41**, 1823–1844 (1996).

10. J. Schmitt, A. Knüttel, and M. Yadlowsky, ''Confocal microscopy in turbid media,'' *J. Opt. Soc. Am. A* **11**, 2226–2235 (1994).

11. S. Prahl, M. Keijzer, S. Jacques, and A. Welch, ''A Monte Carlo model of light propagation in tissues,'' *Dosimetry Laser Rad. Med. Biol.* **5**, 102–111 (1989).

12. U. Haberland, ''Optische Chirp-Kohärenztomographie: Untersuchung an streuenden Medien mit Hilfe durchstimmbarer Laser,'' dissertation, RWTH Aachen, Institut für Hochfrequenztechnik (1997).

13. G. Nilsson, T. Tenland, and P. Öberg, ''A new instrument for continuous measurement of tissue flow by light beating spectroscopy,'' *IEEE Trans. Biomed. Eng.* **27** (1980).